A Three-Dimensional Vertically Aligned Functionalized Multilayer Graphene Architecture: An Approach for Graphene-Based Thermal Interfacial Materials

Qizhen Liang,[†] Xuxia Yao,[†] Wei Wang,[†] Yan Liu,[†] and Ching Ping Wong[†,‡,*]

[†]School of Materials Science and Engineering, Georgia Institute of Technology, 771 Ferst Drive, Atlanta, Georgia 30332, United States, and [‡]College of Engineering, The Chinese University of Hong Kong, Hong Kong

ABSTRACT Thermally conductive functionalized multilayer graphene sheets (fMGs) are efficiently aligned in large-scale by a vacuum filtration method at room temperature, as evidenced by SEM images and polarized Raman spectroscopy. A remarkably strong anisotropy in properties of aligned fMGs is observed. High electrical (~386 S cm^{-1}) and thermal conductivity (~112 W m^{-1} K^{-1} at 25 °C) and ultralow coefficient of thermal expansion (~−0.71 ppm K^{-1}) in the in-plane direction of A-fMGs are obtained without any reduction process. Aligned fMGs are vertically assembled between contacted silicon/silicon surfaces with pure indium as a metallic medium. Thus-constructed three-dimensional vertically aligned fMG thermal interfacial material (VA-fMG TIM) architecture has significantly higher equivalent thermal conductivity (75.5 W m^{-1} K^{-1}) and lower contact thermal resistance (5.1 mm^2 K W^{-1}), compared with their counterpart from A-fMGs that are recumbent between silicon surfaces. This finding provides a throughout approach for a graphene-based TIM assembly as well as knowledge of vertically aligned graphene architectures, which may not only facilitate graphene's application in current demanding thermal management but also promote its widespread applications in electrodes of energy storage devices, conductive polymeric composites, *etc.*

KEYWORDS: alignment · anisotropy · multilayer graphene · thermal interfacial materials · assembly

Low operation temperature and efficient heat dissipation are important for device life and speed in current electronic and photonic technologies. However, gaps between contact solid surfaces, such as silicon dies, metallic heat spreaders, and heat sinks, *etc.*, cause high interfacial thermal resistance, resulting in a major bottleneck of heat dissipation in various devices.[1−4] Gap-filling thermal interfacial materials (TIMs) based on carbon nanomaterials (*e.g.*, carbon nanotubes and carbon nanofibers) were substantially studied in order to handle the bottleneck; however, they are still limited by large contact thermal resistance.[3−7] Graphene, an ultrathin flat membrane from sp^2 carbon atoms, is a novel promising candidate for TIMs in today's electronic and photonic devices.[7,8]

Graphene has extraordinarily high in-plane electrical mobility,[9] thermal conductivity,[8] mechanical strength,[10] and ultralarge specific surface area.[11] Due to these unique properties, within several years since its discovery, graphene has been widely applied in microelectronic devices,[12] chemical sensors,[13] transparent electrically conductive films,[14] electrodes of energy storage devices,[11] and fillers in conductive polymeric composites,[15] *etc.* It is noticed that relative arrangements of graphene in devices are crucial for their multiplex applications. For example, graphene recumbent on solid substrates can be patterned and interconnected for field-effect transistor application.[12,16−18] In contrast, graphene must be stacked in a 3-D porous structure in electrodes of electrical storage devices to facilitate rapid ion dissipation and make full use of its large specific surface area.[11] Therefore, particular arrangements of graphene in various devices are necessary for their diverse functions. For TIM application, efficient heat dissipation and reduced interfacial thermal resistance in the normal direction of contact solid surfaces are desired,[3−6] so that graphene is expected to be vertically stacked between contact solid surfaces. However, as an ultrathin membrane-like material, graphene is susceptible to van der Waals forces and usually tends to be recumbent on substrates. Thereby, direct growth of vertically aligned free-standing graphene on solid substrates in large-scale is difficult

* Address correspondence to cp.wong@mse.gatech.edu.

Received for review November 1, 2010 and accepted February 10, 2011.

Published online March 08, 2011
10.1021/nn200181e

and rarely available in current studies, bringing significant barriers in applying graphene as TIMs.

In this work, it is found that, if aligned and densely packed in an array, multilayer graphene sheets can be self-supported, conveniently rearranged, and vertically assembled between solid surfaces thereafter, circumventing the significant difficulty in direct growth of vertically aligned graphene arrays. In addition, large-volume heat dissipation requires a joint contribution of a large number of graphene sheets. Alignment is crucial in bulk processing of graphene because it orients graphene sheets and optimizes properties of large-scale graphene arrays in their orientation direction. Although direct alignment of pristine graphene in a large-scale array is still absent, previous studies on graphene oxide (GO) and reduced GO indicate that alignment can make best use of their extraordinary in-plane properties. Stankovich *et al.* first prepared paper-like aligned GO with notably high mechanical strength.[19] Chen *et al.* reported a high electrical conductivity of thermally reduced GO paper.[20] However, in-plane thermal conductivity of both GO and reduced GO (1.9 W m^{-1} K^{-1} and 0.14−2.87 W m^{-1} K^{-1}, respectively) is 3 to 4 orders of magnitude lower than pristine graphene.[21,22] Thereby, further efforts on preparation of high thermally conductive graphene-based nanomaterials in large-scale arrays must be addressed.

Here, thermally conductive functionalized multilayer graphene sheets (fMGs) are prepared according to the method reported by Veca *et al.*[23] Thus-prepared fMGs are aligned with a vacuum filtration method at room temperature. An efficient alignment of fMGs is evidenced by SEM images and quantified by polarized Raman spectroscopy according to a "depolarization effect".[24] Strong anisotropies in properties of aligned fMGs (A-fMG) are found. Remarkably high electrical and thermal conductivities as well as ultralow coefficient of thermal expansion (CTE) in the in-plane direction of A-fMGs are obtained without aid of any reduction process. Moreover, a three-dimensional vertically aligned fMG TIM (VA-fMG TIM) architecture is constructed between contacted silicon/silicon surfaces with pure indium as a metallic medium. Significantly higher equivalent thermal conductivity and lower contact thermal resistance of VA-fMG TIMs are obtained, compared with their counterpart from recumbent A-fMGs. This finding provides a throughout approach for a graphene-based TIM assembly as well as knowledge of vertically aligned graphene architectures, which may not only facilitate current demanding thermal management but also promote graphene's widespread applications such as electrodes for energy storage devices, polymeric anisotropic conductive adhesives, *etc*.

RESULTS AND DISCUSSION

Alignment of fMGs. Preparation of paper-like aligned GO by a water filtration method exists.[19] Usually prepared by extreme oxidation of graphite, GO is highly functionalized and soluble in water, facilitating its alignment in water. However, although GO can be electrically conductive after reduction,[20] structural defect level of reduced GO is still high due to permanent damages on the fine lattice structure of graphene, which are introduced by extreme oxidation conditions in GO preparation but cannot be fully recovered by reduction, inevitably debating its thermal conductivity by 3−4 orders of magnitude.[22] In order to obtain a high thermally conductive array, we align reduction-free thermally conductive surface functionalized multilayer graphene sheets (fMGs). According to a method reported by Veca *et al.*,[23] fMGs are prepared in a moderate oxidation environment (mixed sulfuric and nitric acid) with aid of sonication, in contrast with the extreme oxidation conditions in GO preparation.[19−21,25] Thickness of thus-prepared fMGs is mainly centered between 2 and 10 nm with an average of 7.35 nm, as evidenced by an AFM height image in Figure S1 of the Supporting Information. Raman spectra of fMGs in Figure S2 show a 2D peak at ∼2701 ± 6 cm^{-1} with an intensity ranging from 1/3 to half of the G band peak intensity. Moreover, in contrast to an asymmetric 2D peak of graphite at ∼2723 cm^{-1}, the 2D peak of fMGs is symmetric, which can be seen in Supporting Information. As a Raman fingerprint of graphene, 2D peaks are influenced by the electrical structure of graphene.[26] Thereby, oxygen-containing functional groups and defects, which can affect the electrical structure of graphene, have significant impact on the intensity and shape of the 2D peaks, as shown by a low-intensity broad 2D peak of graphene oxide reported by Eda *et al.*[27] Here, the 2D peak of fMGs indicated that their electrical structure is significantly different from that of graphite and graphene oxide. A low defect level of fMGs is also shown by a low D band peak in Figure S2. Nevertheless, as detailed in following results in the study, fMGs are highly thermally conductive, for which no reduction is necessary. This suggests that the fine lattice structure of fMGs is well-maintained, while functional groups are mainly localized within surface domains.

X-ray photoelectron spectra (XPS, Figure S3) show an O1s peak and an asymmetric C1s peak corresponding to conjugated carbon−carbon bonds (284.3 eV), carbon−hydroxyls (285.3 eV), and carboxyls (288.4 eV), compared with the symmetric C1s peaks (284.4 eV) of pristine graphite. FTIR spectrum in Figure S4 confirms the surface functionalization of fMGs by giving peaks at 3448 (−OH), 1380, and 1727 cm^{-1} (C═O). Carboxyls can be ionized by water molecules and generate negative charges on the fMG surface to provide strong electronic repulsion forces,[28] significantly improving dispersion of fMGs in water, as shown in Figure 1a. In a following vacuum filtration process, as illustrated in Figure 1d, a piece of anodic aluminum oxide filtration paper (0.1 μm pore size) holds fMGs on its surface as

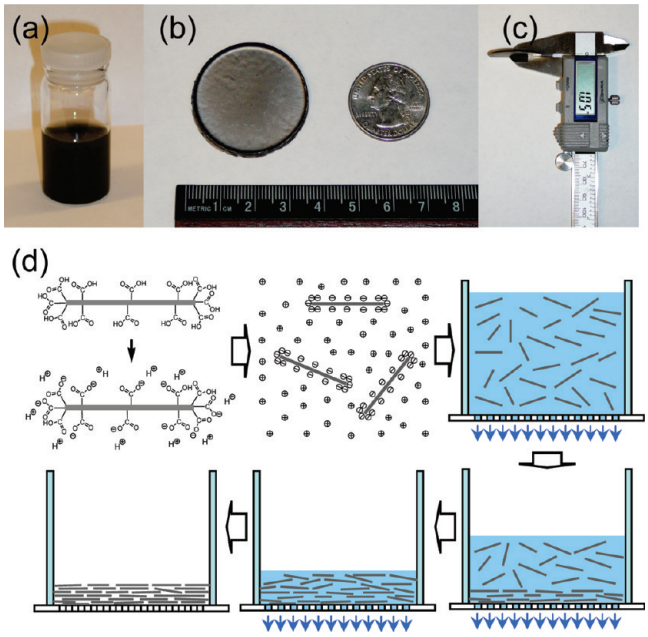

Figure 1. Alignment of fMGs. (a) Well-dispersed fMGs in water. (b) A-fMG sample with a diameter of ~32 mm. (c) A-fMG sample with a thickness of 1.05 mm. (d) Schematic illustration of alignment of fMGs.

water flows down, resulting in the fMGs' conformal orientation along the filtration paper. A filtration cake of aligned fMGs with a density of ~1.6 g cm^{-3}, a diameter of ~32 mm, and a thickness up to 1.05 mm is obtained, as shown by Figure 1b,c.

Characterization of A-fMGs' Alignment. SEM images of A-fMGs in Figure 2 evidence a well-laminated structure of aligned fMGs (A-fMGs), indicating high alignment efficiency. Moreover, polarized Raman spectroscopy is applied to quantify alignment of A-fMGs by measuring sensitivity of G band intensity on polarization geometries according to a "depolarization effect".[24,29−32] As detailed in Figure 3a and Methods, a polarized analyzer is applied to detect backscattering light intensity and set in directions parallel or perpendicular to polarization of the incident laser, which are usually named "VV" (vertical/vertical) and "VH" (vertical/horizontal) configurations. Angle (θ) between polarization of the incident laser and orientation of A-fMGs is applied to describe the polarization geometries. The sensitivity of measured G band intensity on angle θ is studied by an analysis of polarized Raman spectra obtained with different θ (every 10° from 0 to 360°) in both of the configurations. In Figure 3b, measured Raman intensities of the G band in VV configuration show periodical alternations between peaks and valleys every 90°, which are not prominent in the VH configuration. According to a depolarization effect reported by Ajiki *et al.*,[24] during an excitation process of Raman scattering, energy is absorbed by "interband optical transitions" happening only along the vector component parallel to the orientation of polarized phonon carriers. This results in a proportional dependence of absorption intensity (I_A) upon $\cos^2\theta$. Intensity of backscattered laser (I_S) can be considered as proportional to I_A to confirm conversion of energy in an equilibrium state. Moreover, measured Raman intensity scales proportionally to the squared projection of the backscattering electric vector in the polarization direction of the analyzer. Therefore, theoretically, Raman intensities of G band in VV and VH configurations "$I_{VV}(\theta)$" and "$I_{VH}(\theta)$" should obey the following equations.

$$I_{VV}(\theta) = I_{VV}(0°)\cos^4\theta \quad (1)$$

$$\frac{I_{VV}(\theta)}{I_{VH}(\theta)} = \frac{\cos^4\theta}{\cos^2\theta\sin^2\theta} \quad (2)$$

Thus, applying the G band intensity when θ is equal to 0° in the VVconfiguration, $I_{VV}(0°)$, as a reference, relative Raman intensities for VV and VH configurations at G band, $I_{R,VV}(\theta)$ and $I_{R,VH}(\theta)$, are theoretically equal to $\cos^4\theta$ and $\cos^2\theta\sin^2\theta$, respectively. The dependence of $I_{R,VV}(\theta)$ on $\cos^4\theta$ explains its significant reducing trend as angle θ changes from 0 to 90° in Figure 3c. In contrast, measured $I_{R,VH}(\theta)$ showed a much smoother value changing from 0.276 to 0.313, with a broad peak at ~50° within a range from 0 to 90°, showing a much weaker fluctuation corresponding to its theoretical value of $\cos^2\theta\sin^2\theta$. Depolarization ratio ($I_{VV}(90°)/I_{VV}(0°)$) of G band intensity in the VV configuration is 0.276 ± 0.06, comparable to 0.204 (calculated from $I_{VV}(0°)/I_{VV}(90°) = 4.9$) for a fiber from aligned single-walled carbon nanotubes,[29] suggesting an efficient alignment of fMGs.

Anisotropy of A-fMGs. A strong anisotropy of A-fMGs is evidenced by a distinguished contrast between in-plane ($\alpha_{\parallel}$, ~−0.71 ppm K^{-1}) and cross-plane ($\alpha_{\perp}$, 70.4 ppm K^{-1}) coefficient of thermal expansion (CTE) shown by Figure 4b. Although cross-plane CTE of A-fMGs is found to be

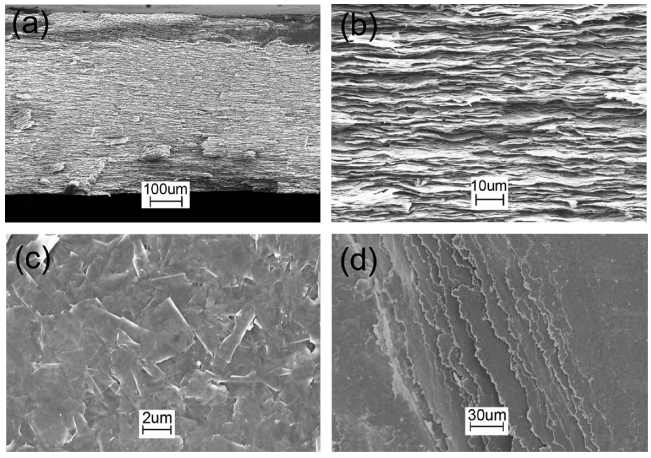

Figure 2. SEM images of A-fMGs. (a) SEM image of a cross-section surface. (b) Magnified SEM image of a cross-section surface. (c) Top view of A-fMGs under SEM. (d) SEM image of a broken A-fMG surface with gradient.

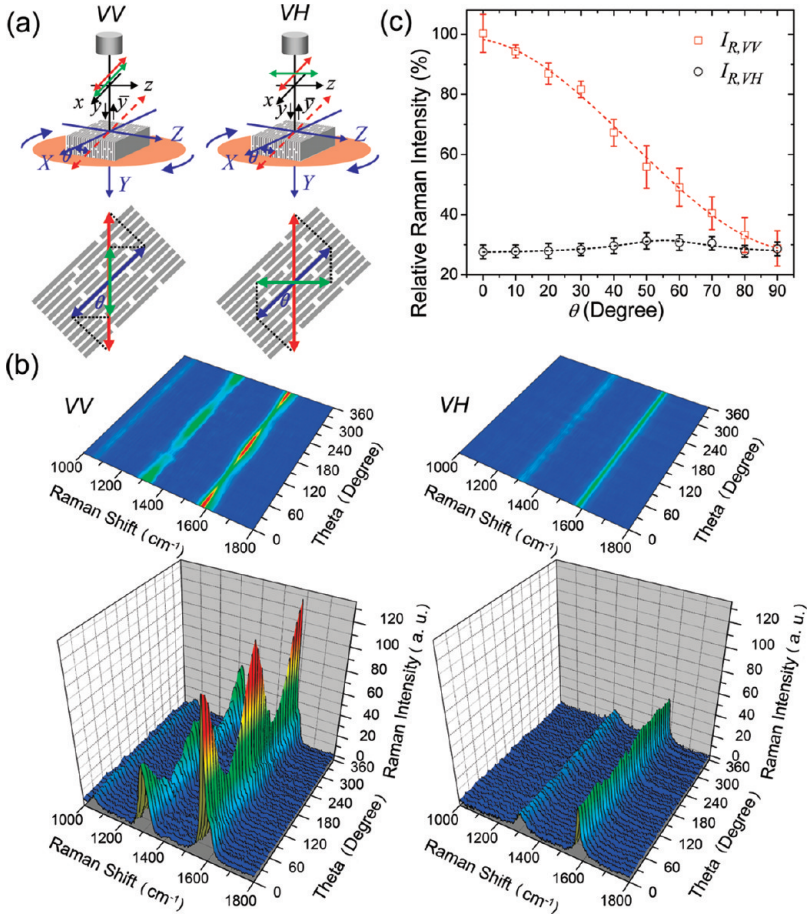

Figure 3. Polarized Raman spectra of A-fMGs. (a) Schematic illustrations of VV and VH configurations. Orientation of fMGs, polarization directions of incidental light, and analyzer are shown by the blue, red, and green double arrows, respectively. Black arrows (*x*,*y*,*z*) denote the three axles in the absolute coordinate system, while the blue arrows show two in-plane directions (*X* and *Y*) and cross-plane direction (*Z*) of A-fMGs, respectively; θ is the angle between polarization of incident light and fMG orientation. (b) Three-dimensional illustration of measured Raman intensity for VV and VH polarization configurations. (c) Relative G band (1581 cm^{-1}) intensity as a function of angle θ of A-fMGs in VV and VH configurations.

larger than that of the *c* axis in a fine graphite lattice at room temperature (~28 ppm K^{-1})[33] due to a relatively loose packing of A-fMGs, the result is compatible with reported low in-plane CTE values (~−2 ppm K^{-1}) along the *a* axis of graphite crystallite and axle direction of carbon nanotubes.[33,34] Furthermore, by giving an in-plane

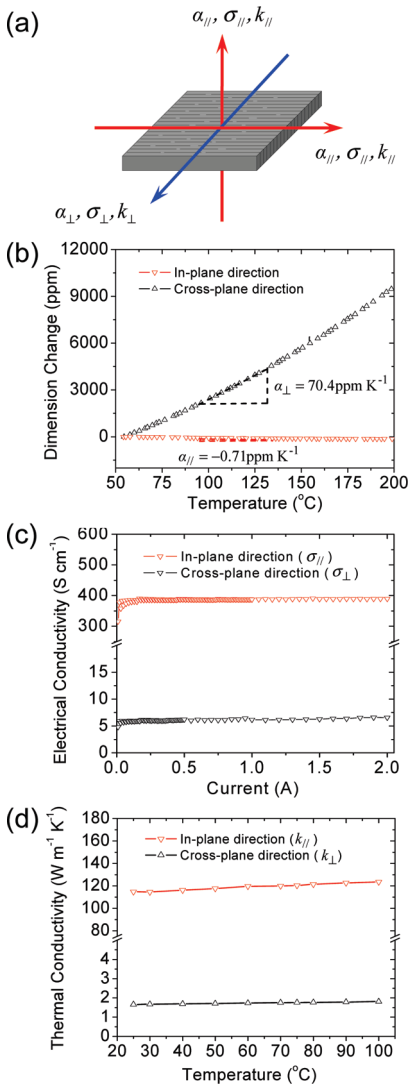

Figure 4. Anisotropies of A-fMGs. (a) Schematic illustration of in-plane and cross-plane CTE, electrical and thermal conductivity of A-fMGs. (b) Thermal mechanical analysis of A-fMGs. Slopes of the curves are in-plane and cross-plane coefficients of thermal expansion (CTEs), respectively. (c) In-plane and cross-plane electrical conductivity of A-fMGs at room temperature. (d) In-plane and cross-plane thermal conductivity of A-fMGs.

electrical conductivity ($\sigma_{||}$) of ~386 S cm^{-1} and a cross-plane electrical conductivity ($\sigma_{\perp}$) of ~6.1 S cm^{-1} in Figure 4c, A-fMGs show an even stronger anisotropy ($\sigma_{||}/\sigma_{\perp}$ = 63.3 at 25 °C) of electrical conductivity than that of vertically aligned carbon nanotube arrays ($\rho_{\perp}/\rho_{||}$ is smaller than 10 at room temperature).[35] Moreover, a distinct contrast between in-plane thermal conductivity ($k_{||}$, between 112 and 123 W m^{-1} K^{-1}) and cross-plane thermal conductivity ($k_{\perp}$, from 1.62 to 1.81 W m^{-1} K^{-1}) suggests that an efficient alignment can optimize in-plane thermal conductivity of aligned fMGs to a remarkable degree ($k_{||}/k_{\perp}$ = 69.3 at 25 °C). In-plane sketching phonon mode E_{2g}, which usually corresponds to the G band in Raman spectra, has a dominating function in thermal transfer along graphene.[8,29−32] A high sensitivity of G band on angle θ in the VV configuration in polarized Raman spectra indicates that orientation of fMGs is statistically narrow-distributed, facilitating a ballistic phonon transport and a high thermal conductivity in the in-plane direction of A-fMGs.

Assembly of A-fMG TIM Architectures. Three-dimensional TIM architectures are constructed by assembling A-fMGs between Si/Si joint surfaces with a thin layer (~10 μm) of pure indium as a metal medium. As illustrated in Figure 5a, A-fMG samples are carefully sliced, rearranged, and sandwiched between thus-prepared Si wafers with the orientation of fMGs parallel or perpendicular to Si surfaces, corresponding to RA-fMG and VA-fMG TIM assemblies, respectively. RA-fMG TIM assembly is found to be vulnerable to mechanical shake and fails in a standard drop test of reliability, while VA-fMG TIM assembly passes the tests without detachment, indicating a significantly better interfacial adhesion between VA-fMGs and Si substrates.

Equivalent thermal diffusivity (α_{TIM}) of both TIM assemblies is measured by a light flash apparatus (LFA 447 NanoFlash, Netzsch Thermal Analysis). A sophisticated analysis software (Proteus LFA Analysis, Netzsch Thermal Analysis) with a mathematical model designed for triple-layer sandwich samples is applied in measuring equivalent thermal diffusivities of A-fMG TIMs (α_{TIM}) by experimentally collecting and mathematically fitting the nonlinear regression of data signal with consideration of heat loss. Equivalent thermal conductivity (k_{TIM}, estimated from $k_{TIM} = \alpha_{TIM}\rho_{TIM}C_{p,TIM}$) includes effects of interfacial thermal resistance across the A-fMGs/In/Si multiple interface (RA-fMGs/In/Si) and intrinsic thermal resistance of A-fMGs (T/k), as shown in the following equation.

$$R_{TIM} = \frac{BLT}{k_{TIM}} = 2R_{A\text{-}fMGs/In/Si} + \frac{T}{k}$$

where R_{TIM}, BLT, k_{TIM}, $R_{A\text{-}fMGs/In/Si}$, T, and k represent total thermal resistance across TIMs, bond line thickness of TIMs, equivalent thermal conductivity of TIMs, thermal resistance across A-fMGs/In/Si multiple interfaces, thickness of A-fMGs in the TIM architecture, and thermal conductivity of A-fMGs in the corresponding direction, respectively.

As detailed in Methods and Supporting Information, equivalent thermal conductivity of the described RA-fMG TIMs and VA-fMG TIMs are 1.39 and 75.5 W m^{-1} K^{-1}, respectively. In a comparison shown in Figure 5b, we notice that equivalent thermal conductivity of VA-fMG TIMs is almost 2 orders of magnitude higher than that of RA-fMG TIMs. Moreover, thermal resistance values ($R_{AfMGs/In/Si}$) across A-fMGs/In/Si multiple interfaces in RA-fMG and VA-fMG TIMs are 42.5 and 5.1 mm^2 K W^{-1}, respectively. At least two reasons should be counted for better adhesion and lower $R_{AfMGs/In/Si}$ of VA-fMG TIMs.

First, interfacial thermal conductance between substrates and graphitic nanomaterials (*e.g.*, carbon nanotubes) can be significantly improved by

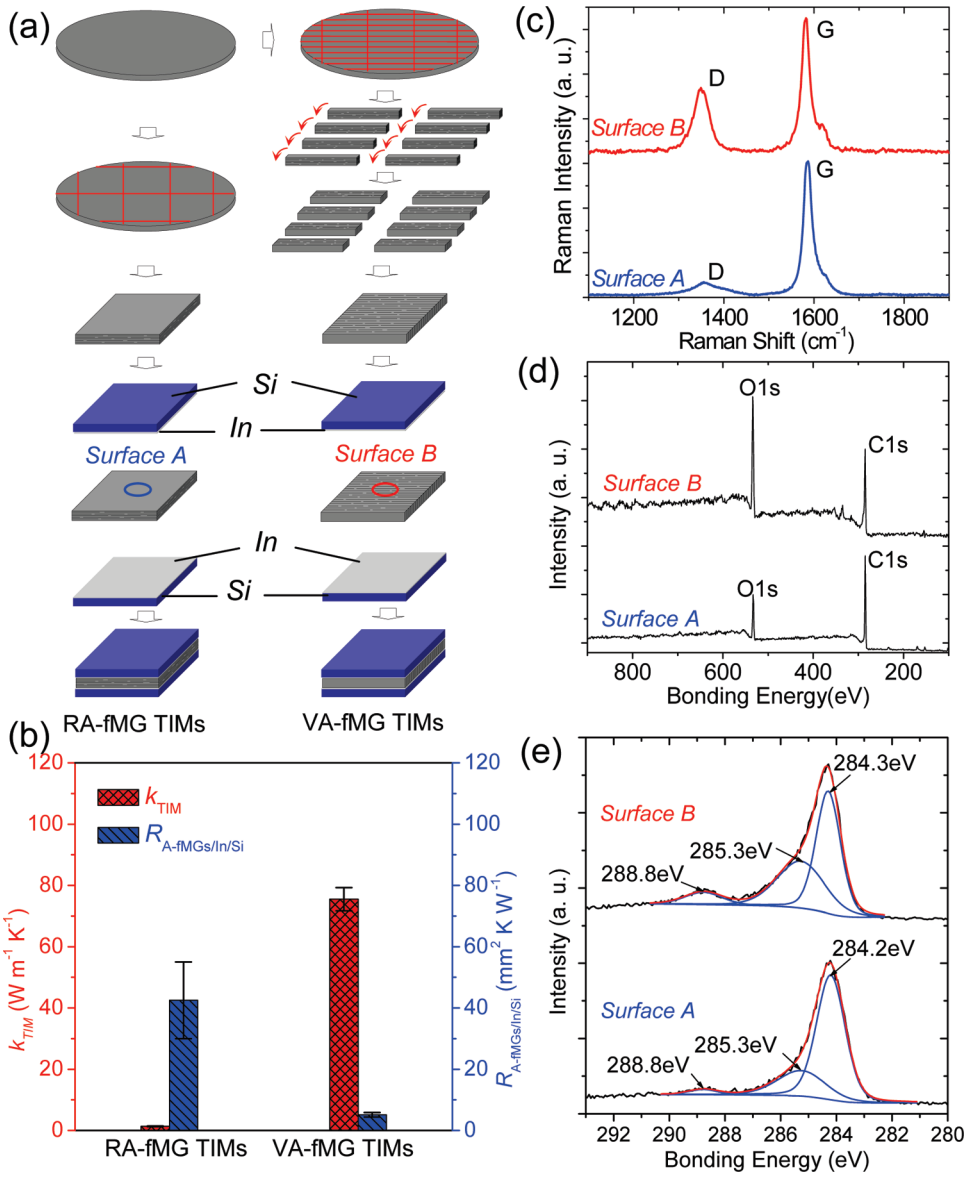

Figure 5. Assembly of A-fMG TIM architectures. (a) Schematic illustration of RA-fMG and VA-fMG TIM assemblies. (b) Contrast of equivalent thermal conductivity (k_{TIM}) and interfacial thermal resistance across A-fMGs/In/Si interface ($R_{A\text{-}fMGs/In/Si}$) between RA-fMG and VA-fMG TIM assemblies. (c) Comparison between Raman spectra of the side-wall (surface A) and cross-section surface (surface B) of A-fMGs. (d) Comparison between low-resolution scanning XPS spectra of surface A and B. (e) Comparison of high-resolution XPS spectra between surface A and B.

molecular-level interfacial chemical bonding.[36] Indium is capable of forming relatively stable chemical bonds with carboxyls, as demonstrated by an affinity between indium and various carboxylic acids in indium extraction.[37,38] Both simulation studies and experimental results indicate that carboxyls on graphene are concentrated on edge domains.[39−41] Compatible with that reported, a relatively higher concentration of carboxyls on A-fMGs cross-section surface is evidenced. Here, Raman spectra in Figure 5c indicated a higher defect level of cross-section surface (surface B) of A-fMGs than that on a side-wall surface (surface A), corresponding to concentration of fMG edges. Low-resolution scanning XPS spectra in Figure 5d show a significantly higher concentration (∼33.8%) of oxygen atoms on surface B than that (∼17.7%) on surface A, as shown by a calculation in Supporting Information according to the empirical atomic sensitivity factors for O1s and C1s (0.66 and 0.25, respectively) reported by Wagner *et al.*[42] Moreover, high-resolution XPS spectra in Figure 5e confirm a higher concentration of carboxyl on surface B, by giving a integrated area ratio (49:41:10) among conjugated carbon−carbon bonds (284.3 eV), carbon−hydroxyl bonds (285.3 eV), and carbonyl bonds (∼288.4 eV) of surface B, compared with that (71:27:2) of surface A. Arrangement of VA-fMG TIMs can make a best use of carboxyls' aggregation on the cross-section surface in the joint between VA-fMGs and indium, as illustrated in Figure 6, resulting in reduced $R_{A-fMGs/In/Si}$ and improved adhesion to indium-coated Si substrates.

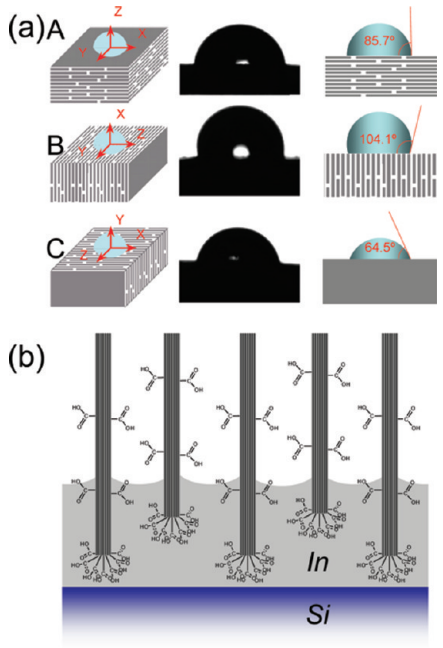

Figure 6. VA-fMG TIM architecture facilitates a significant reduction of $R_{A\text{-}fMGs/In/Si}$. (a) Contact angle measurements in three different three-dimensional geometries, as detailed in Methods. (b) Schematic illustration of a VA-fMGs/In/Si multiple interface junction.

Second, it is noticed that metal's filling can dramatically increase contact surface area between metal and carbon nanomaterials and significantly contribute to an enhanced adhesion. For example, filling open-ended carbon nanotubes with metals (*e.g.*, Pd) has been substantially reported.[43−45] Zhu *et al.*[46] reported that adhesion between metallic solder and carbon nanotubes is significantly improved by opening the ends of vertically aligned carbon nanotubes. Here, compliant with a laminated structure shown in SEM images in Figure 2, a unique anisotropic wetting phenomenon of water indicates the existence of microchannels on a cross-section surface of A-fMGs. As shown by Figure 6a and Methods, the contact angle of deionized water on A-fMGs is measured in three geometries. Compared to geometry A (contact angle is equal to 85.7°), geometries B and C give significantly different contact angle values of 104.1 and 67.5°, respectively. In order to show the phenomena, water droplets must be influenced by two physical effects due to microchannels on the cross-section surface of A-fMGs along fMGs' orientation (*X* and *Y* directions in Figure 6a). On the one hand, the existence of microchannels increases surface roughness along the *Z* direction, resulting in enlarged contact angle of water in geometry B by a "lotus effect", which has been observed on a superhydrophobic surface from a patterned vertically aligned CNT.[47,48] On the other hand, capillary forces along thin microchannels among A-fMGs and hydrophilic functionalizations on fMGs are responsible for a reduced contact angle in geometry C.[45] In VA-fMG TIMs, cross-section surfaces of A-fMGs with microchannels are right faced to indium-coated silicon substrates, facilitating filling of melted indium, as shown schematically in Figure 6b. This can efficiently increase contact surface area between indium and A-fMGs, resulting in an improved adhesion and reduced contact thermal resistance in VA-fMG TIM assembly.

Comparison with Reported Results. Graphene is a promising candidate in TIM application due to its extraordinarily high thermal conductivity (~5300 W m^{-1} K^{-1} for suspended monolayer graphene and ~600 W m^{-1} K^{-1} for supported monolayer graphene).[8,49] However, large-volume heat dissipation requires a joint contribution of a large number of graphene sheets. Graphene sheets must be aligned in a large-scale array in order to meet the requirements for TIM applications. Valuable efforts have been paid on preparation of aligned graphene oxide (GO) by thermally reduced GO paper.[19,20] However, in-plane thermal conductivity of GO and reduced GO (1.9 and 0.14−2.87 W m^{-1} K^{-1}, respectively) is relatively low and unlikely able to meet demanding requirements in the thermal management of current photonic and electronic devices.[21,22] Moreover, toxic reduction agents (*e.g.*, hydrazine) and high temperatures (400−1100 °C) applied in chemical or thermal reduction of graphene oxide[11,14,20] are not preferred in real industrial applications. This work is an approach for the alignment of reduction-free thermally conductive functionalized multilayer graphene in large-scale. High electrical ($\sigma_{\|}$, ~386 S cm^{-1}) and thermal conductivities ($k_{\|}$, between 112 and 123 W m^{-1} K^{-1}) as well as ultralow CTE ($\alpha_{\|}$, ~−0.71 ppm K^{-1}) in the in-plane direction of A-fMGs are obtained without the aid of a reduction process.

Moreover, graphene is usually recumbent on solid substrates, while vertically aligned graphene architecture on a solid substrate is rarely available and less studied. However, for TIMs, electrodes of ultracapacitors, *etc.*, efficient heat dissipation, and electrical conductance in the normal direction of solid surfaces are strongly desired.[3−7,50] Significant advantages of a 3D vertically aligned fMG architecture in TIM application are demonstrated here. Equivalent thermal conductivity of VA-fMG TIMs can be almost 2 orders of magnitude higher than that of RA-fMG TIMs. Contact thermal resistance ($R_{AfMGs/In/Si}$) across the A-fMGs/In/Si multiple interface in VA-fMG TIMs (5.1 mm^2 K W^{-1}) is significantly lower than that of RA-fMG TIMs (42.5 mm^2 K W^{-1}).

Nevertheless, it is noticed that equivalent thermal conductivity of TIMs based on vertically aligned carbon nanotubes (CNTs) and carbon nanofibers (CNFs) is relatively low due to a high contact thermal resistance between CNTs/CNFs and substrates.[6,7] Ngo *et al.*[5] applied contact measurement techniques and obtained an interfacial thermal resistance of

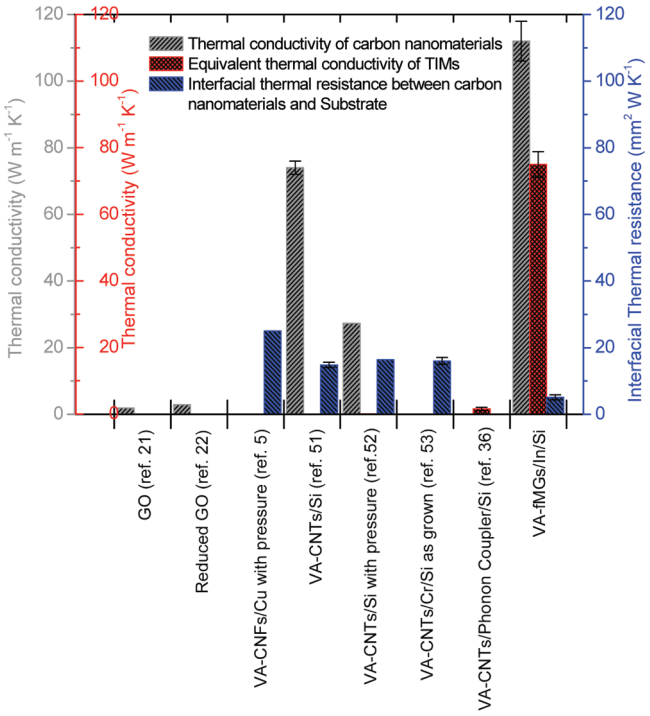

Figure 7. Comparison of thermal conductivity of carbon nanomaterials, effective (equivalent) thermal conductivity of their TIMs, and contact (interfacial) thermal resistance between carbon nanomaterials and substrates in reported structures (refs 5, 21, 22, 36, 51, 52, and 53) with results in this work.

$\sim$25 mm^2 K W^{-1} between a vertically aligned carbon nanofiber array and a copper substrate at an assembling pressure of 60 psi. Wang *et al.*[51] used a photothermal method and obtained absolute and effective thermal conductivity of a vertically aligned CNT (VACNT) array grown on Si substrate as $\sim$27.3 and $\sim$0.145 W m^{-1} K^{-1}, respectively, as well as a thermal interfacial resistance of $\sim$16.4 mm^2 K W^{-1} across a CNT/Cr/Si multiple interface. Hu *et al.*[52] applied 3-omega measurements on an as-grown VACNT structure at 100 kPa pressure and reported an effective thermal conductivity of the CNT arrays and contact thermal resistance between CNTs and Si as $\sim$74 W m^{-1} K^{-1} and $\sim$15 mm^2 K W^{-1}, respectively. Cola *et al.*[53] reported that a contact thermal resistance between VACNTs and Si scales $\sim$15.8 mm^2 K W^{-1} by photoacoustic characterization. Lin *et al.*[36] applied molecular phonon couplers between VACNTs and Si and reported that an equivalent thermal conductivity of thus-prepared VACNT TIM structure measured by laser flash method is $\sim$1.6 W m^{-1} K^{-1}. As illustrated in Figure 7, VA-fMG TIMs have high thermal conductivity and low contact thermal resistance, suggesting their promising potentials in current demanding thermal management for electronic and photonic devices.

CONCLUSIONS

Here, we summarize the efforts to prepare a 3D vertically aligned functionalized multilayer graphene architecture between silicon surfaces and an exploration of their application as TIMs. A high alignment efficiency of "reduction-free" conductive fMGs is evidenced by SEM and polarized Raman spectroscopy. Strongly anisotropic CTE and electrical and thermal conductivity of A-fMGs are observed. Remarkably high electrical and thermal conductivities as well as ultralow coefficient of thermal expansion (CTE) in the orientation direction of aligned fMGs (A-fMGs) are obtained, without any reduction process. VA-fMG TIMs showed a high equivalent thermal conductivity up to 75.5 W m^{-1} K^{-1} and low thermal resistance cross VA-fMGs/In/Si interface (5.1 mm^2 K W^{-1}), suggesting their promising potentials in thermal management of electronic and photonic applications.

METHODS

Alignment. The fMGs are synthesized according to a method reported by Veca *et al.*[23] Thus-prepared fMGs (0.8 g) are dispersed in 1 L of deionized water and vacuum-filtrated with a 47 mm vacuum filtration system equipped with an anodic aluminum oxide (AAO) filtration paper (0.1 μm pore size, Anodisc 47, Whatman International Ltd.). The obtained filtration cake is carefully washed by DI water, removed from filtration paper, and dried at 105 °C for 3 h.

Polarized Raman Spectroscopy. A HoloLab series 5000 modular Raman spectroscope (Kaiser Optical Systems Inc.) equipped with a 785 nm laser is applied. Polarization of incident light is fixed. As illustrated by Figure 3a, a rotatable stage is set perpendicular to incidental light. An A-fMG sample is vertically stood on the

rotatable stage in a way that incidental light is parallel to the orientation of A-fMGs. In order to detect the backscattering light intensity, a polarized analyzer is set in directions parallel or perpendicular to the polarization of the incident light, which are named VV and VH configurations, respectively.

Property Measurements. In-plane ($\alpha_{\parallel}$) and cross-plane ($\alpha_{\perp}$) coefficients of thermal expansion (CTE) of A-fMGs are tested by a thermo-mechanical analyzer (TA Instruments, 2940) with a temperature increase rate of 5 °C min^{-1} from room temperature to 250 °C and a force of 0.1 Newton. TA Instruments Advantage 2004 software is applied to estimate CTEs of A-fMGs with an equation of $\alpha = (\partial L/\partial T)/L$, where L and T represent dimension and temperature. In the test, A-fMG samples are set vertically or recumbently on a quartz stage, corresponding to their in-plane ($\alpha_{\parallel}$) and cross-plane ($\alpha_{\perp}$) coefficient of thermal expansion (CTE), respectively. Current−voltage response of an A-fMG sample was measured on a Keithley 2000 multimeter equipped with a two-point probe testing stage. Electrical conductivity is calculated from obtained current−voltage data and sample dimensions. Values of thermal conductivity are calculated from the equation $k = \alpha\rho C_p$, where k, α, ρ, and C_p reprensent thermal conductivity, thermal diffusivity, material density, and heat capacity, respectively. Thermal diffusivities of A-fMGs are measured by a light flash apparatus (LFA 447 NanoFlash, Netzsch Thermal Analysis). Density is calculated from sample weight and dimensions. Heat capacity is tested by a differential scanning calorimeter (TA Instruments, 2920) with a temperature increase rate of 5 °C min^{-1} from room temperature to 100 °C.

TIM Assembly. Si wafers (1 mm × 1 mm) are coated with melted pure indium at 180 °C. Thickness of the indium coating is ~10 μm after careful polishing at room temperature. A-fMG samples are sliced and sandwiched between thus-prepared Si wafers with an orientation of fMGs parallel or perpendicular to the contacted Si surfaces, corresponding to RA-fMG and VA-fMG TIM assemblies, respectively. The sandwiched samples are clamped with small pressure (~0.02 MPa) and placed in a convection oven at 200 °C for 20 min and cooled to room temperature. No pressure is applied in equivalent thermal conductivity measurements of thus-prepared TIMs.

Contact Angle Tests. As shown by Figure 6a, contact angle tests are conducted on A-fMGs in three geometries. (A) A water droplet (1 μL) is dropped on a sample surface which is parallel to both *X* and *Y* axles but perpendicular to the *Z* axle; then contact angle is measured from a view angle parallel to *X* axle (or *Y*, which is identical with *X* axle in this case). (B) A water droplet (1 μL) is dropped on a cross-section surface of A-fMGs. Then contact angle is measured from a view angle parallel to *X* axle. (C) A water droplet (1 μL) is dropped on a same surface as geometry B, but contact angle is measured from a view angle parallel to *Z* axle.

Acknowledgment. The authors would like to acknowledge the National Science Foundation (NSF CMMI Nos. 0621115 and 0422553) for financial support of this work. Moreover, the authors appreciate generous help of Prof. Mohan Srinivasarao (School of Materials Science and Engineering, Georgia Institute of Technology) in polarized Raman spectroscopy measurement. We also appreciate Dr. Lingbo Zhu (Dow Chemical Co.) and Dr. Yonghao Xiu (Intel Co.) for instructive discussions.

Supporting Information Available: (1) An AFM height image of A-fMG surface and corresponding thickness information. (2) A comparison of Raman spectra between graphite and fMGs. (3) A comparison of X-ray photoelectronics spectra between pristine graphite and fMGs. (4) FTIR spectrum of fMGs. (5) Thermal conductivity measurement of assembled A-fMGs TIMs. This material is available free of charge *via* the Internet at http://pubs.acs.org.

REFERENCES AND NOTES

1. Stan, M. R.; Burleson, W. P. Bus-Invert Coding for Low Power I/O. *IEEE Trans. VLSI Syst.* **1995,** *3*, 49–58.
2. Borkar, S. Y. Design Challenges of Technology Scaling. *IEEE Micro.* **1999,** *19*, 23–29.
3. Tong, T.; Zhao, Y.; Delzeit, L.; Kashani, A.; Meyyappan, M.; Majumdar, A. Dense, Vertically Aligned Multiwalled Carbon Nanotube Arrays as Thermal Interfacial Materials. *IEEE Trans. Compon. Packag. Technol.* **2007,** *30*, 92–100.
4. Xu, J.; Fisher, T. S. Enhancement of Thermal Interface Materials with Carbon Nanotube Arrays. *Int. J. Heat Mass Transfer* **2006,** *49*, 1658–1666.
5. Ngo, Q.; Cruden, B. A.; Cassell, A. M.; Sims, G.; Meyyappan, M.; Li, J.; Yang, C. Y. Thermal Interface Properties of Cu-Filled Vertically Aligned Carbon Nanofiber Arrays. *Nano Lett.* **2004,** *4*, 2403–2407.
6. Prasher, R. Thermal Interface Materials: Historical Perspective, Status, and Future Directions. *Proc. IEEE* **2006,** *94*, 1571–1586.
7. Prasher, R. Graphene Spreads the Heat. *Science* **2010,** *328*, 185–186.
8. Balandin, A. A.; Ghosh, S.; Bao, W.; Calizo, I.; Teweldebrahn, D.; Miao, F.; Lau, C. N. Superior Thermal Conductivity of Single-Layer Graphene. *Nano Lett.* **2008,** *8*, 902–907.
9. Geim, A. K.; Novoselov, K. S. The Rise of Graphene. *Nat. Mater.* **2007,** *6*, 183–191.
10. Lee, C.; Wei, X. D.; Kysar, J. W.; Hone, J. Measurement of the Elastic Properties and Intrinsic Strength of Monolayer Graphene. *Science* **2008,** *321*, 385–388.
11. Stoller, M. D.; Park, S. J.; Zhu, Y. W.; An, J. H.; Ruoff, R. S. Graphene-Based Ultracapacitors. *Nano Lett.* **2008,** *8*, 3498–3502.
12. Novoselov, K. S.; Geim, A. K.; Morozov, S. V.; Jiang, D.; Zhang, Y.; Dubonos, S. V.; Grigorieva, I. V.; Firsov, A. A. Electric Field Effect in Atomically Thin Carbon Films. *Science* **2004,** *306*, 666–669.
13. Fowler, J. D.; Allen, M. J.; Tung, V. C.; Yang, Y.; Kaner, R. B.; Weiller, B. H. Practical Chemical Sensors from Chemically Derived Graphene. *ACS Nano* **2009,** *3*, 301–306.
14. Becerril, H. A.; Mao, J.; Liu, Z.; Stoltenberg, R. M.; Bao, Z.; Chen, Y. Evaluation of Solution-Processed Reduced Graphene Oxide Films as Transparent Conductors. *ACS Nano* **2008,** *2*, 463–470.
15. Dikin, D. A.; Stankovich, S.; Zimney, E. J.; Piner, R. D.; Dommett, G. H. B.; Evmenenko, G.; Nguyen, S. T.; Ruoff, R. S. Functionalized Graphene Sheets for Polymer Nanocomposites. *Nature* **2007,** *448*, 457–460.
16. Avouris, P.; Chen, Z.; Perebeinos, V. Carbon-Based Electronics. *Nat. Nanotechnol.* **2007,** *2*, 605–613.
17. Berger, C.; Song, Z. M.; Li, T. B.; Li, X. B.; Ogbazghi, A. Y.; Feng, R.; Dai, Z. T.; Marchenkov, A. N.; Conrad, E. H.; First, P. N..;*et al.*Ultrathin Epitaxial Graphite: 2D Electron Gas Properties and a Route toward Graphene-Based Nanoelectronics. *J. Phys. Chem. B* **2004,** *108*, 19912–19916.
18. Robinson, J. A.; LaBella, M.; Trumbull, K. A.; Weng, X. J.; Cavelero, R.; Daniels, T.; Hughes, Z.; Hollander, M.; Fanton, M.; Snyder, D. Epitaxial Graphene Materials Integration: Effects of Dielectric Overlayers on Structural and Electronic Properties. *ACS Nano* **2010,** *4*, 2667–2672.
19. Stankovich, S.; Dikin, D. A.; Dommett, G. H. B.; Kohlhaas, K. M.; Zimney, E. J.; Zimney, E. J.; Stach, E. A.; Piner, R. D.; Nguyen, S. T.; Ruoff, R. S. Preparation and Characterization of Graphene Oxide Paper. *Nature* **2007,** *442*, 282–286.
20. Chen, H.; Muller, M. B.; Gilmore, K. J.; Wallace, G. G.; Li, D. Mechanically Strong, Electrically Conductive, and Biocompatible Graphene Paper. *Adv. Mater.* **2008,** *20*, 3557–3561.
21. Wei, Z. Q.; Wang, D. B.; Kim, S.; Kim, S.-Y.; Hu, Y. K.; Yakes, M. K.; Laracuente, A. R.; Dai, Z. T.; Marder, S. R.; Berger, C..;*et al.*Nanoscale Tunable Reduction of Graphene Oxide for Graphene Electronics. *Science* **2010,** *328*, 1373–1376.
22. Schwamb, T.; Burg, B. R.; Schirmer, N. C.; Poulikakos, D. An Electrical Method for the Measurement of the Thermal and Electrical Conductivity of Reduced Graphene Oxide Nanostructures. *Nanotechnology* **2009,** *20*, 405704.
23. Veca, L. M.; Meziani, M. J.; Wang, W.; Wang, X.; Lu, F. S.; Zhang, P. Y.; Lin, Y.; Fee, R.; Connell, J. W.; Sun, Y. P. Carbon Nanosheets for Polymeric Nanocomposites with High Thermal Conductivity. *Adv. Mater.* **2009,** *21*, 2088–2092.
24. Ajiki, H.; Ando, T. Aharonov-Bohm Effect in Carbon Nanotubes. *Physica B* **1994,** *201*, 349–352.
25. Hummers, W. S.; Offeman, J. R. E. Preparation of Graphitic Oxide. *J. Am. Chem. Soc.* **1958,** *80*, 1339–1339.

26. Ferrari, A. C.; Meyer, J. C.; Scardaci, V.; Casiraghi, C.; Lazzeri, M.; Piscanec, S.; Jiang, D.; Novoselov, K. S.; Roth, S.; Geim, A. K. Raman Spectrum of Graphene and Graphene Layers. *Phys. Rev. Lett.* **2006,** *97*, 187401.
27. Eda, G.; Chhowalla, M. Chemically Derived Graphene Oxide: Towards Large-Area Thin-Film Electronics and Optoelectronics. *Adv. Mater.* **2010,** *22*, 2392–2415.
28. Li, D.; Muller, M. B.; Gilje, S.; Kaner, R. B.; Wallace, G. G. Processable Aqueous Dispersions of Graphene Nanosheets. *Nat. Nanotechnol.* **2008,** *3*, 101–105.
29. Gommans, H. H.; Alldredge, J. W.; Tashiro, H.; Park, J.; Magnuson, J. Fibers of Aligned Single-Walled Carbon Nanotubes: Polarized Raman Spectroscopy. *J. Appl. Phys.* **2000,** *88*, 2509–2514.
30. Reich, S.; Thomson, C. Raman Spectroscopy of Graphite. *Philos. Trans. R. Soc. London, Ser. A* **2004,** *362*, 2271–2288.
31. Rao, A. M.; Jorio, A.; Pimenta, M. A.; Dantas, M. S. S.; Saito, R.; Dresselhaus, G.; Dresselhaus, M. S. Polarized Raman Study of Aligned Multiwalled Carbon Nanotubes. *Phys. Rev. Lett.* **2000,** *84*, 1820–1823.
32. Saito, R.; Jorio, A.; Souza, A. G.; Dresselhaus, G.; Dresselhaus, M. S.; Pimenta, M. A. Probing Phonon Dispersion Relations of Graphite by Double Resonance Raman Scattering. *Phys. Rev. Lett.* **2002,** *88*, 027401.
33. Tsang, D. K. L.; Marsden, B. J.; Fok, S. L.; Hall, G. Graphite Thermal Expansion Relationship for Different Temperature Ranges. *Carbon* **2005,** *43*, 2902–2906.
34. Maniwa, Y.; Fujiwara, R.; Kira, H.; Tou, H.; Kataura, H.; Suzuki, S.; Achiba, Y.; Nishibori, E.; Takata, M.; Sakata, M..;*et al.* Thermal Expansion of Single-Walled Carbon Nanotube (SWNT) Bundles: X-ray Diffraction Studies. *Phys. Rev. B* **2001,** *64*, 241402.
35. de Heer, W. A.; Bacsa, W. S.; Chatelain, A.; Gerfin, T.; Humphrey-Baker, R.; Forro, L.; Ugarte, D. Aligned Carbon Nanotube Films—Production and Optical and Electronic-Properties. *Science* **1995,** *268*, 845–847.
36. Lin, W.; Zhang, R.; Moon, K. S.; Wong, C. P. Molecular Phonon Couplers at Carbon Nanotube/Substrate Interface To Enhance Interfacial Thermal Transport. *Carbon* **2010,** *48*, 107–113.
37. Danilov, N. A.; Krylov, Yu. S.; Korpusov, G. V.; Kostikova, G. V.; Barabanov, I. R.; Bezrukov, L. B.; Kornoukhov, V. N.; Novikova, G. Ya.; Yanovich, E. A.; Nesterova, N. P..;*et al.*A Study of Indium Extraction with Carboxylic Acids with the Aim To Produce Scintillators for Solar Neutrino Detection by LENS Spectroscopy of Low-Energy Neutrino. *Radiochemistry* **2005,** *47*, 487–493.
38. Rajesh, N.; Subramanian, M. S. Extractive Separation and Determination of Thallium and Indium by Liquid Scintillation Counting. *Analyst* **1994,** *119*, 2071–2074.
39. Jiang, D. E.; Sumpter, B. G.; Dai, S. How Do Aryl Groups Attach to a Graphene Sheet?. *J. Phys. Chem. B* **2006,** *47*, 23628–23632.
40. Kim, J.; Cote, L. J.; Kim, F.; Yuan, W.; Shull, K. R.; Huang, J. Graphene Oxide Sheets at Interfaces. *J. Am. Chem. Soc.* **2010,** *132*, 8180–8186.
41. Yuge, R.; Zhang, M. F.; Tomonari, M.; Yoshitake, T.; Iijima, S.; Yudasaka, M. Site Identification of Carboxyl Groups on Graphene Edges with Pt Derivatives. *ACS Nano* **2008,** *2*, 1865–1870.
42. Wagner, C. D.; Davis, L. E.; Zeller, M. V.; Taylor, J. A.; Raymond, R. H.; Gale, L. H. Empirical Atomic Sensitivity Factors for Quantitative-Analysis by Electron-Spectroscopy for Chemical-Analysis. *Surf. Interface Anal.* **1981,** *3*, 211–225.
43. Ajayan, P. M.; Iijima, S. Capillary-Induced Filling of Carbon Nanotubes. *Nature* **1993,** *361*, 333–334.
44. Ajayan, P. M.; Ebbesen, T. W.; Ichihashi, T.; Iijima, S. Opening Carbon Nanotubes with Oxygen and Implications for Filling. *Nature* **1993,** *362*, 522–525.
45. Dujardin, E.; Ebbesen, T. W.; Hiura, H.; Tanigaki, K. Capillary and Wetting of Carbon Nanotubes. *Science* **1994,** *265*, 1850–1852.
46. Zhu, L. B.; Sun, Y. Y.; Hess, D. W.; Wong, C. P. Well-Aligned Open-Ended Carbon Nanotube Architectures: An Approach for Device Assembly. *Nano Lett.* **2006,** *6*, 243–247.
47. Xiu, Y. H.; Zhu, L. B.; Hess, D. W.; Wong, C. P. Biomimetic Creation of Hierarchical Surface Structures by Combining Colloidal Self-Assembly and Au Sputter Deposition. *Langmuir* **2006,** *22*, 9676–9681.
48. Zhu, L. B.; Xiu, Y. H.; Xu, J.; Tamirisa, P. A.; Hess, D. W.; Wong, C. P. Superhydrophobicity on Two-Tier Rough Surfaces Fabricated by Controlled Growth of Aligned Carbon Nanotube Arrays Coated with Fluorocarbon. *Langmuir* **2005,** *21*, 11208–11212.
49. Seol, J. H.; Jo, I.; Moore, A. L.; Linday, L.; Aitken, Z. H.; Pettes, M. T.; Li, X. S.; Yao, Z.; Huang, R.; Broido, D..;*et al.*Two-Dimensional Phonon Transport in Supported Graphene. *Science* **2010,** *328*, 213–216.
50. Futaba, D. N.; Hata, K.; Yamaha, T.; Hiraoka, T.; Hayamizu, Y.; Kakudate, Y.; Tanaike, O.; Hatori, H.; Yumura, M.; Iijima, S. Shape-Engineerable and Highly Densely Packed Single-Walled Carbon Nanotubes and Their Applications as Super-Capacitor Electrodes. *Nat. Mater.* **2006,** *5*, 987–994.
51. Wang, X. W.; Zhong, Z. R.; Xu, J. Noncontact Thermal Characterization of Multiwall Carbon Nanotubes. *J. Appl. Phys.* **2005,** *97*, 064302.
52. Hu, X. J.; Padilla, A. A.; Xu, J.; Fisher, T. S.; Goodson, L. E. 3-Omega Measurements of Vertically Oriented Carbon Nanotubes on Silicon. *J. Heat Transfer* **2006,** *128*, 1109–1113.
53. Cola, B. A.; Xu, J.; Cheng, C. R.; Xu, X. F.; Fisher, T. S.; Hu, H. P. Photoacoustic Characterization of Carbon Nanotube Array Thermal Interfaces. *J. Appl. Phys.* **2007,** *105*, 054313.